

Article

Influence of the Gas Flow Rate on the Crack Formation of AlCoCrNi High-Entropy Metallic Film Fabricated Using Magnetron Sputtering

Young-Soon Kim ^{1,†}, Hae-Jin Park ^{1,†}, Young-Seok Kim ², Sung-Hwan Hong ¹  and Ki-Buem Kim ^{1,*} 

¹ Department of Nanotechnology and Advanced Materials Engineering, Sejong University, 209, Neungdong-ro, Gwangjin-gu, Seoul 05006, Republic of Korea; keen95@naver.com (Y.-S.K.); haejinp@sejong.ac.kr (H.-J.P.); shhong@sejong.ac.kr (S.-H.H.)

² R&D Center, APIs Co., 76, Deokcheon-ro 48 beon-gil, Manan-gu, Anyang 14088, Republic of Korea; ysgin82@gmail.com

* Correspondence: kbkim@sejong.ac.kr; Tel.: +82-2-34083690

† These authors contributed equally to this work.

Abstract: In the present study, the AlCoCrNi high-entropy metallic film was deposited on a Si wafer using a magnetron sputtering system. To capture the effects of the sputtering parameters on the microstructure and mechanical properties of the film, the flow rate of Ar gas injected into the chamber (5, 7, and 8 sccm) was controlled. All films were identified as being of BCC phase with compositions of near equiatomic proportions, regardless of the gas flow rates. Nano-scale clusters were observed on the surfaces of all films, and nano-cracks were found in the film deposited at the Ar gas flow rate of 8 sccm, unlike the films deposited at the gas flow rates of 5 and 7 sccm. Detailed microstructural analysis of film deposition at an Ar gas flow rate of 8 sccm indicated that the void boundaries contribute to the formation of nano-cracks. The nano-indentation results indicated that the Ar gas flow rate 5 sccm specimen, with the smallest cluster size at the topmost surface, showed the highest hardness (12.21 ± 1.05 GPa) and Young's modulus (188.1 ± 11 GPa) values.

Keywords: high-entropy metallic film; Ar gas flow rate; shadowing effect; crack; mechanical properties



Citation: Kim, Y.-S.; Park, H.-J.; Kim, Y.-S.; Hong, S.-H.; Kim, K.-B. Influence of the Gas Flow Rate on the Crack Formation of AlCoCrNi High-Entropy Metallic Film Fabricated Using Magnetron Sputtering. *Coatings* **2024**, *14*, 144. <https://doi.org/10.3390/coatings14010144>

Academic Editor: Alberto Palmero

Received: 29 December 2023

Revised: 15 January 2024

Accepted: 17 January 2024

Published: 21 January 2024



Copyright: © 2024 by the authors. Licensee MDPI, Basel, Switzerland. This article is an open access article distributed under the terms and conditions of the Creative Commons Attribution (CC BY) license (<https://creativecommons.org/licenses/by/4.0/>).

1. Introduction

High-entropy alloys (HEAs), unlike conventional alloys, are alloys that combine many elements, and they have attracted a lot of attention as a new concept. Initially reported by Cantor et al. [1] and Yeh et al. [2], HEAs are alloys of five or more elements developed with nearly equimolar ratios. The basic design concept of high-entropy alloys is that, due to high configurational entropy, it is easier to form simple phases such as solid solutions instead of complex phases, and so these alloys have lower free energy and higher phase stability [3–8]. Owing to the differences in the atomic sizes of each element consisting of alloys, high-entropy alloys are generally regarded to have a distorted lattice structure and sluggish diffusion [4,9]. For these reasons, high-entropy alloys show excellent properties such as high hardness, oxidation resistance, irradiation resistance, corrosion resistance, and wear resistance. Therefore, they have attracted attention in various fields such as structural materials, hard coatings, diffusion barriers, and energy materials [10–14].

Surface coating technology is used in various industries to enhance the mechanical properties and corrosion resistance of substrate materials [15–17]. Many studies have investigated binary or ternary film, but traditional metal oxide, carbide, and nitride films have not been able to meet the increasing requirements of such materials. As such, scholars have started to research HEA films to achieve improved thermal and mechanical properties [3,18–24].

HEA films can be developed using various deposition methods, including sputtering, spraying, and laser cladding [25,26]. Meanwhile, as one of the most common vapor

deposition methods, magnetron sputtering deposition is a frequently used technique for forming thin films. With magnetron sputtering, it is known to be easy to control the stoichiometry of thin films by adjusting the target chemical compositions. Also, the quality of thin films can be improved by controlling variables such as input power, gas flow rate, reactive gas, substrate temperature, and deposition time.

However, when the thin film is formed using magnetron sputtering, the shadowing effect can lead to crack formation, and Figure 1 shows a schematic diagram of the shadowing effect. During the film deposition, particles can approach the surface at typical angles and can be selectively accumulated by a higher surface area with a protuberance due to the shadowing effect. This effect leads to the formation of rougher surfaces and void boundaries with columnar structures [27,28]. This phenomenon finally results in crack formation and a reduction in the mechanical properties.

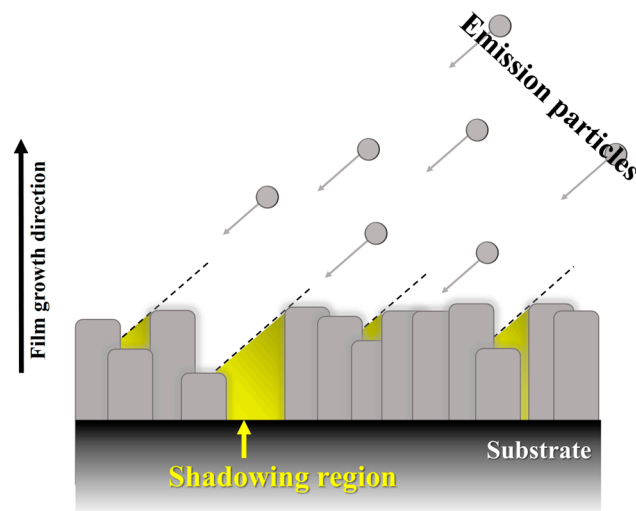


Figure 1. The schematic illustration of the Shadowing effect.

Some studies reported that it possible to control crack formation by raising the substrate temperature during sputtering [29,30]. M. Hu et al. [29] confirmed that cracks gradually disappeared as a result of depositing FeCoNiCrMn HEA metallic film while controlling the substrate temperature from 293 K to 773 K. It can be seen that sufficient diffusion to make a denser thin film was achieved by regulating the substrate temperature [29,30]. However, it is possible to affect the mechanical properties adversely due to phase transformation or the alleviation of defects when the film is formed at a high substrate temperature during the process [21–33]. Other methods that can increase the diffusion energy of the thin film during the sputtering process include bias control of the substrate, gas flow rate control, and working power control.

Our previous study optimized sputtering parameters without phase transformation by systemically controlling variables such as the nitrogen flow ratio and process pressure in the quaternary AlCoCrNi HEN systems [22]. Based on this understanding, we focused on correlating the crack formation and adjusted the Ar gas flow rates of the AlCoCrNi HEA metallic film system in this study. In other words, this study aimed to understand the effect of gas flow rate, which is one of the sputtering parameters that can control diffusion energy during the sputtering process of crack formation and the mechanical properties of the HEA metallic thin film. The Ar gas flow rate was selected to regulate the microstructure of the AlCoCrNi metallic films, on which cracks form under certain conditions. From the results shown in Table 1, it is confirmed that as the Ar gas flow rate increased, the operating pressure also increased. In other words, higher operating pressure decreased the mean free path and energy of the sputter particles.

Due to the mean free path being short when the Ar gas flow rate is high, the mobility of the target particles is substantially decreased before the particles emitted from the target

reach the substrate, thus resulting in a reduced peening effect. On the other hand, the mean free path is long when the Ar gas flow rate is low, and so particles reach the substrate with high mobility and the peening effect can be significant [22,34,35]. Herein, the effect of Ar gas flow rate on microstructure and mechanical properties was investigated in the sputtering process, and the mechanism of crack formation was discussed.

Table 1. The deposition conditions of the AlCoCrNi HEA metallic films.

Composition	Substrate Temperature	Rotation Speed (RPM)	D.C. Power (W)	Base Pressure (Torr)	Operating Pressure (Pa)	Deposition Time (min)	Ar Flow Rate (sccm)
AlCoCrNi	R.T.	10	300	6×10^{-5}	0.37	60	5
					0.44		7
					0.47		8

2. Materials and Methods

2.1. Sample Preparation

The AlCoCrNi metallic films were deposited on Si wafer substrates using a direct current magnetron sputtering system (KCMC Minutus magnetron sputter) at room temperature. Prior to this, p-type Si wafers for the substrate were cleaned for 5 min each with acetone and ethanol to remove impurities on their surfaces utilizing an ultrasonic wave washer. AlCoCrNi (Plansee SE, 25/25/25/25 at.%), the used powder alloy target, had a diameter of 50.8 mm and a thickness of 6.35 mm. The distance between the target and the substrate was 80 mm; the rotational speed of the substrate was fixed at 10 RPM for the uniform deposition of the coating layer. The vacuum chamber was initially evacuated down to around 6×10^{-5} Torr before introducing sputter gas, while operating pressure was 0.37 Pa, 0.44 Pa, and 0.47 Pa, respectively. The change in processing pressure with varying argon gas flow rates in the sputtering chamber is shown in Table 1. Then, the flow rate of high purity argon gas (99.999%) was controlled using a mass flow controller (MFC) (MKS, Andover, MA, USA). The Ar gas flow rate was controlled from 5 sccm to 8 sccm at a fixed applied power of 300 W. The present conditions for the deposition of the AlCoCrNi metallic films are summarized in Table 1. The deposition time was fixed at 60 min, and it was set empirically to achieve micron-scale thickness. The pre-sputtering was conducted for 10 min at 300 W in 20 sccm prior to deposition in order to minimize any contamination from the target surface and ensure a reproducible target surface state before each deposition.

2.2. Microstructure Characterization

The topmost surface images and cross-sectional fracture surface images, along with the thickness and chemical compositions of the as-deposited Al-Co-Cr-Ni HEA metallic thin films, were characterized by a field emission scanning electron microscope (FE-SEM, SU-8010, Hitachi, Tokyo, Japan) equipped with an energy-dispersive X-ray spectrometer at a 20 kV operating voltage. The cross-section of the sample was prepared by cleaving off the film from a single-crystal silicon substrate. The thickness and fracture surface of the metallic films were measured with FE-SEM. The metallic film thickness after being deposited for an hour was about 1700–1900 nm. For EDS measurement, different regions were measured more than four times at 2.5 k magnification for each specimen. The crystal structure of the thin film was characterized using an X-ray diffractometer (XRD, PANalytical/Empyreal/PC, Malvern, UK) with Cu target $K_{\alpha 1}$ radiation ($\lambda = 1.5406 \text{ \AA}$). Further, the average grain size were calculated via the Scherrer equation using the FWHM (full width at half maximum) of the dominant peak in the measured XRD [36].

For a more detailed microstructural and chemical analysis of the coating layer, the transmission electron microscope (TEM, Tecnai F20 G2, FEI, Hillsboro, OR, USA) was used. The selected area electron diffraction (SAED) pattern and the high-resolution cross-sectional surface were also confirmed using TEM at an accelerating voltage of 200 kV. Focused ion beam (FIB, Hitach-NX5000, Tokyo, Japan) thinning was conducted with Ga^+ ions to prepare

the AlCoCrNi thin-film specimens for TEM analysis. Digital Micrograph software version 3.10.1 (Gatan Inc., Pleasanton, CA, USA) was used to analysis and process the TEM images. The surface morphology and RMS (root-mean-square) roughness were measured using an atomic force microscope (AFM, hpAFM, Nanomagnetics Instrument, Oxford, UK) in contact mode with a $2 \times 2 \mu\text{m}^2$ scan area with a resolution of 256×256 pixels.

2.3. Mechanical Properties

The mechanical properties were measured at room temperature (25 °C) using a nano-indenter (NHT-X, CSM, Needham, MA, USA) equipped with a Berkovich diamond tip. Load–displacement curves were evaluated according to Oliver and Pharr [37]. The depth control mode was used, the loading and unloading rates were both fixed at 10 mN/m, and the pause time was fixed at 0 s. To ensure that the reliability of the mechanical properties was not affected by the substrate, the displacement was adjusted to 1/10 of the film thickness during the nanoindentation test. Indentation was performed at least 10 times, and the average value was measured while excluding the maximum and minimum values.

3. Results and Discussion

3.1. Phase Analysis and Microstructure Characterization of Thin Films

The XRD patterns of AlCoCrNi HEA metallic films deposited at various Ar gas flow rates are shown in Figure 2. Due to the thin deposition thickness, even the XRD pattern of the Si substrate was detected, and aside from the peak of the Si substrate, only the peak of the AlCoCrNi metallic film was exclusively analyzed. The XRD result confirmed that the phase of the AlCoCrNi HEA metallic films is the BCC phase. It appears that there is no phase transformation of the thin films according to the Ar gas flow control during the sputtering process. The grain size of the HEA metallic thin films was calculated from the Scherrer equation [36], using the dominant peak from the measured XRD in scans with a 2θ range of 20 to 80° . The calculated grain sizes are summarized in Table 2. This increase in the grain size with an Ar gas flow rate of 5 sccm is due to the decline in the collisional events during the travel of the particles from the target to the substrate. So, particles reach the substrate with promoted mobility caused by the long mean free path of sputtered atoms [22,38,39], resulting in a highly crystalline film. These results act as factors influencing mechanical properties.

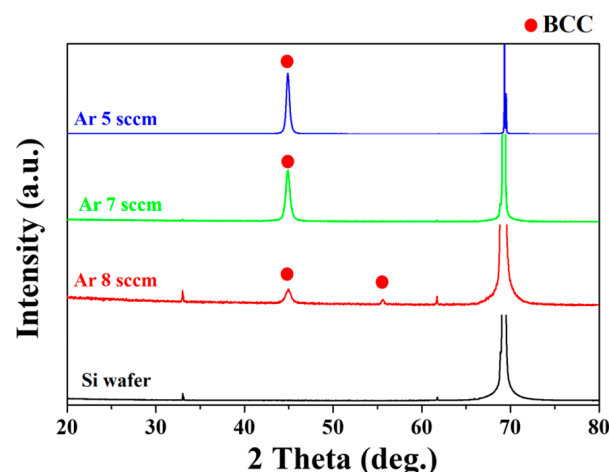


Figure 2. The X-ray diffraction (XRD) patterns of the AlCoCrNi HEA metallic films deposited under various Ar gas flow rates.

Table 2. The roughness, cluster size, and grain size of the AlCoCrNi HEA metallic films deposited at various Ar gas flow rates.

Composition	Condition	R_{rms} (nm)	Cluster Size (nm)	Grain Size (nm)
AlCoCrNi	5 sccm	0.77 ± 0.03	38.16 ± 1.79	20.14 ± 0.2
	7 sccm	0.87 ± 0.04	75.76 ± 5.71	15.24 ± 0.5
	8 sccm	2.71 ± 0.16	86.21 ± 3.33	13.35 ± 0.7

For detailed phase characterization, TEM SAED pattern analysis was conducted on AlCoCrNi HEA metallic films deposited at Ar gas flow rates of 5 sccm or 8 sccm. For both thin films, SAED pattern analysis was performed in three sections—top layer (A), middle layer (B), and bottom layer (C), respectively—as shown in Figure 3. As shown in Figure 3a, the SAED pattern analysis of regions A, B, and C revealed that the entire film was composed of the BCC phase (reference circle shown $a = 2.88 \text{ \AA}$) in reasonable agreement with XRD measurements. Therefore, it can be confirmed that the thin film achieved uniform growth, and the same result is seen in the case of Figure 3b.

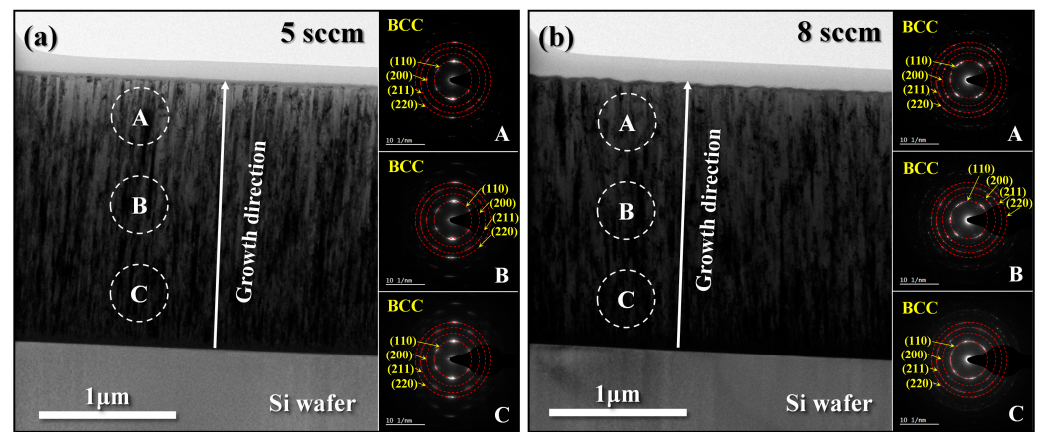
**Figure 3.** The bright-field (BF) images of the AlCoCrNi HEA metallic films deposited under Ar gas flow rates of (a) 5 sccm and (b) 8 sccm and the corresponding SAED pattern obtained from regions A, B, and C in (a,b).

Figure 4 shows the chemical composition of the AlCoCrNi metallic films obtained via FE-SEM energy-dispersive X-ray spectroscopy (EDS). The atomic ratio of each element of Al, Co, Cr, and Ni has a value between 24.4 at.% and 25.6 at.%, showing that the chemical composition of the deposited films is very similar to the target composition, with almost equiatomic percentages at various Ar gas flow rates. The detailed chemical composition of the target materials and thin films is also summarized in Table 3. As all the elements were deposited in a similar ratio to the composition of the target, sufficient energy was applied to obtain different sputtering yields for each component [21,40–42].

Table 3. The quantitative values of chemical composition of each element of the AlCoCrNi metallic films.

		Elements (at. %)			
		Al	Co	Cr	Ni
Target materials		24.94	25.09	24.76	25.21
Ar flow rate (sccm)	5	24.64	25.42	24.75	25.31
	7	24.43	25.57	24.84	25.17
	8	24.92	25.52	24.52	25.05

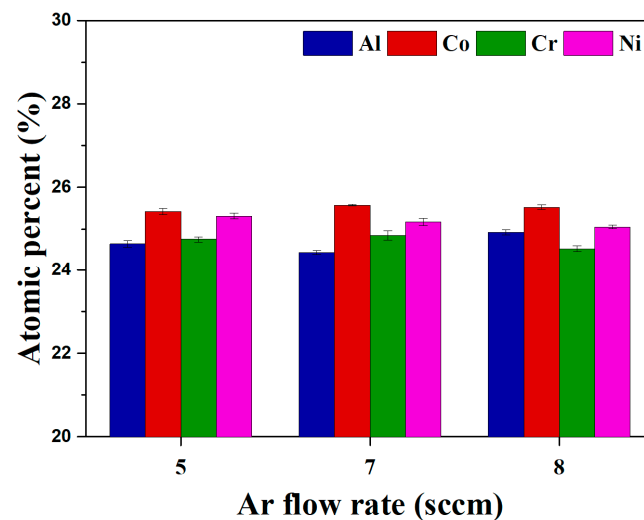


Figure 4. The energy-dispersive X-ray spectroscopy (EDS) results of the AlCoCrNi HEA metallic films produced under various Ar gas flow rates.

Cross-sectional and top-surface FE-SEM images and TEM high-resolution images of AlCoCrNi HEA metallic films deposited at various Ar gas flow rates are displayed in Figure 5a–j. From the cross-sectional images of each specimen in Figure 5a,e,g, the columnar structure of the thin film, which is characteristic of sputtering, can be clearly identified. Further, there is no significant difference in the thickness of the coating layer, and it can be observed that there is little difference in the deposition rate as well. While there was no difference in the cross-sectional images of the thin films, a difference could be found clearly in the topmost surface of thin films. From Figure 5b,f,h, it can be observed that the size of the clusters increases along with the Ar gas flow rate. The cluster size was determined using the diameter measurement method [43] and listed in Table 2. Moreover, in the specimen with an Ar gas flow rate of 8 sccm, cracks occurred along the cluster boundaries. The reason that these cracks occurred is that sufficient diffusion energy was not applied to fill the empty space caused by the shadowing effect [29,30,38,39,44]. Owing to the shorter mean free path caused by the relatively higher gas flow rate, the particles protruding from the target during sputtering were decelerated as they reached the substrate, so the atomic peening effect appeared to be reduced [22,34,35]. As shown in Figure 5h, it can be seen that the crack propagated along the large agglomerates. The propagation of cracks along this cluster is schematically shown in Figure 5k. For detailed microstructure analysis, cross-sectional high-resolution TEM image analysis was performed on specimens deposited at the Ar gas flow rates of 5 sccm and 8 sccm, respectively, and the results are shown in Figure 5c,d,i,j. The columnar growth directions are indicated by white arrows, and all films exhibit a nano-columnar growth shape. Figure 5d,j are enlarged images, corresponding to the square sections in (a) and (g), respectively. In the specimen deposited at an Ar gas flow rate of 8 sccm, void boundaries indicated by yellow arrows were clearly identified, and in the specimen deposited at an Ar gas flow rate of 5 sccm, no void boundaries were found. From Figure 5h, it can be concluded that sufficient diffusion energy was not applied during the sputtering and that the porous structure by the void boundaries caused surface crack formation.

The topmost surface AFM images and topography of AlCoCrNi HEA metallic films deposited at different Ar gas flow rates are shown in Figure 6. These can be used as supporting information for analyzing the results of the FE-SEM images. Comparing the y -axis scale of the topography of the 8 sccm specimen in Figure 6f with those of other specimens in Figure 6b,d shows a noticeable difference caused by forming cracks. Table 2 lists the values of the roughness, cluster size, and grain size of the HEA metallic thin films to confirm the correlations among the readings shown in it.

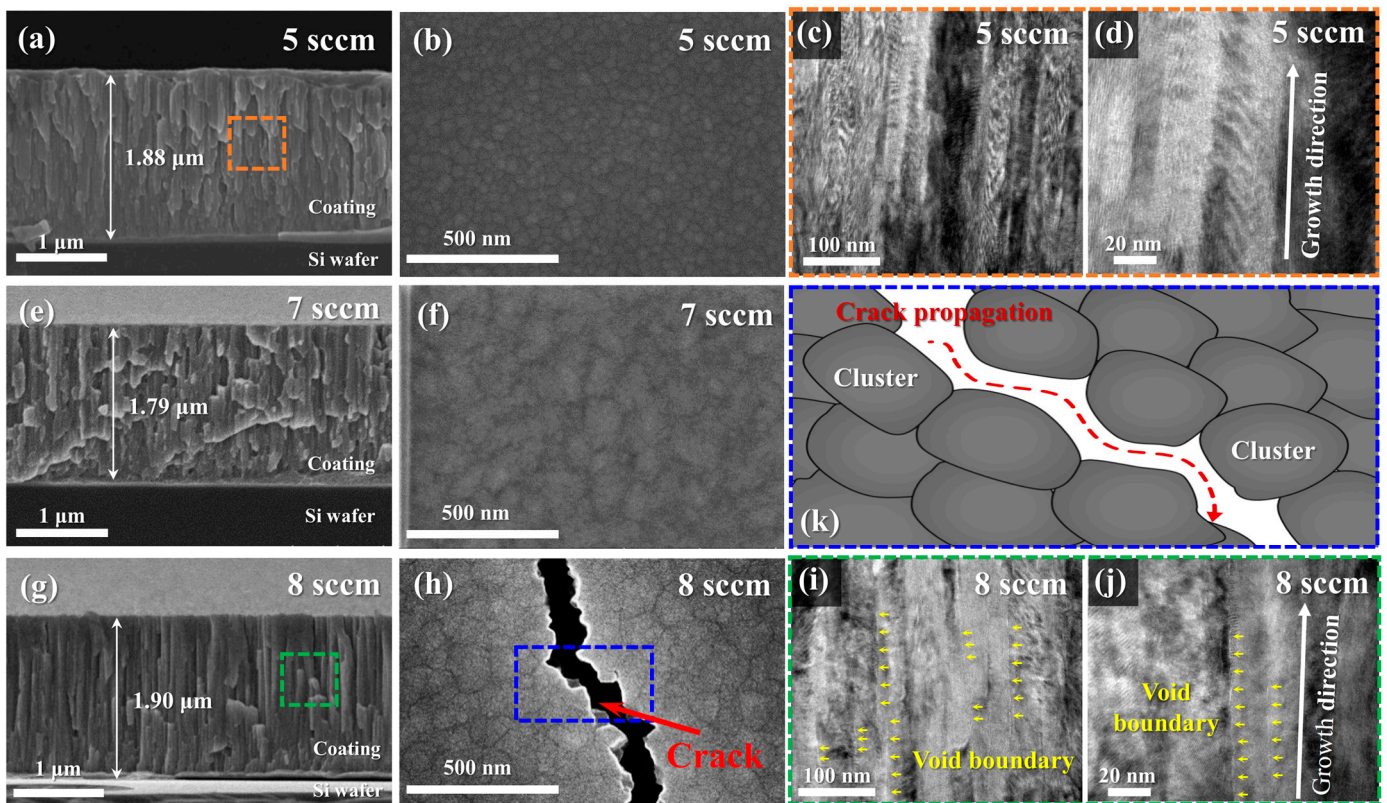


Figure 5. The cross-sectional and surface FE-SEM and TEM high-resolution (HR) images of the AlCoCrNi metallic films deposited at various Ar gas flow rates: (a–d) 5 sccm, (e,f) 7 sccm, (g–j) 8 sccm; (k) schematic diagram of the topmost surface corresponding to the square section (blue line) on (h).

The AlCoCrNi HEA metallic film specimen with an Ar gas flow rate of 8 sccm shows a higher roughness value, and it is considered that the surface roughness rapidly increased due to the porous structure as it reached the critical point of the Ar gas flow where cracks are formed.

In other words, the sputtered particles experience more collisions before reaching the substrate at a higher flow rate and pressure. More collisions can lead to the agglomeration of sputtered particles while traveling to the substrate. That is, sputtered particles will arrive at the substrate with varying sizes; this nonuniformity can lead to higher roughness values. Similar to the increasing trend of roughness, the cluster size also increases according to the Ar gas flow rate, which is consistent with the propagation of cracks to the empty space at the boundaries of the clusters.

The increase in surface roughness is linked to the growth in cluster size at a higher Ar gas flow rate, which is considered to significantly contribute to crack formation. That is, a larger number of atomic collisions results in a higher rate of scattering of sputtered particles. Therefore, a high gas flow rate over an optimized level increases the atomic penetration depth, contributing to crack formation eventually.

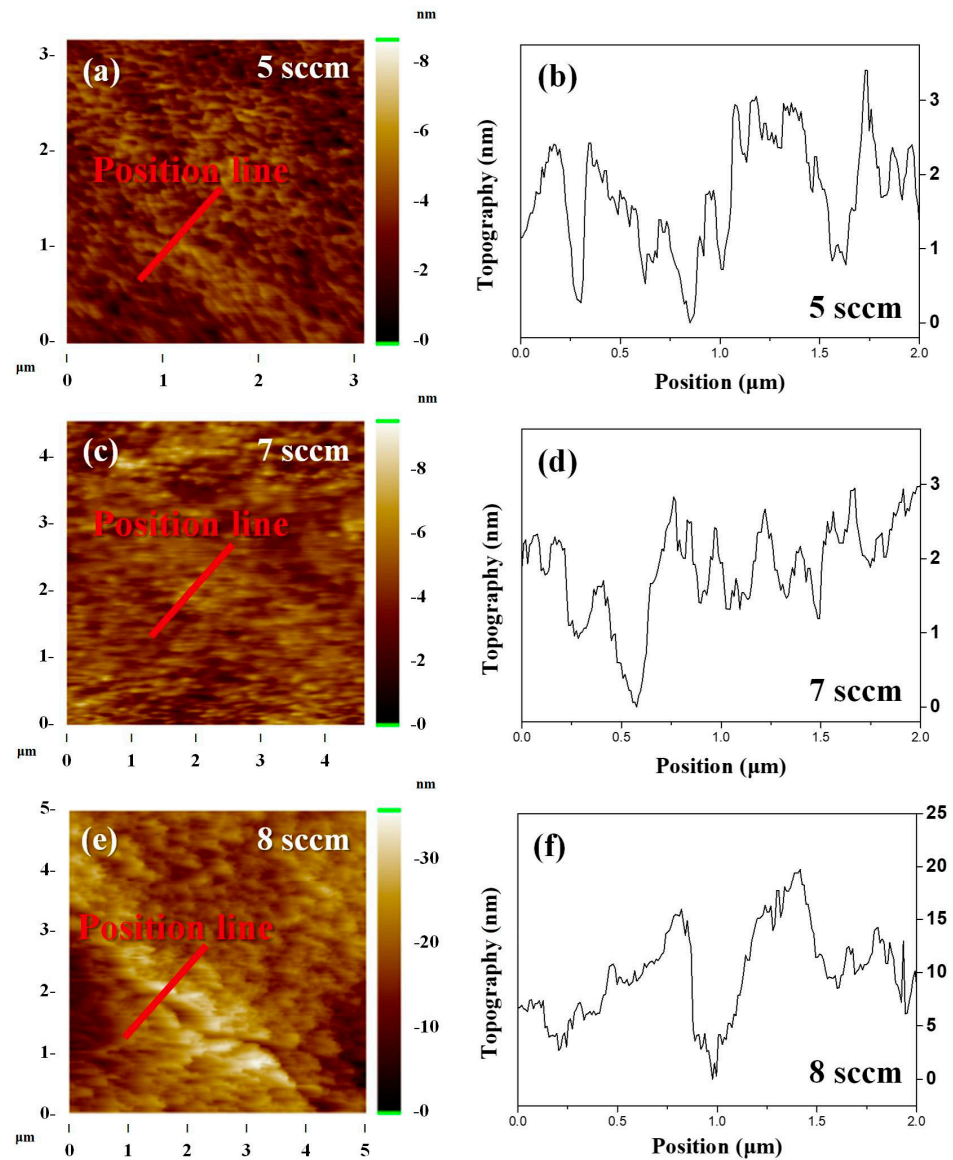


Figure 6. The AFM images and topography of AlCoCrNi HEA metallic films deposited at various Ar gas flow rates of (a,b) 5 sccm, (c,d) 7 sccm, and (e,f) 8 sccm.

3.2. Nanoindentation Test

Nanoindentation testing was performed on the topmost surface of AlCoCrNi HEA metallic films to investigate Ar gas flow rate-dependent mechanical properties, such as the hardness (H_{IT}), Vickers hardness (HV_{IT}), and Young's modulus (E_{IT}) of the thin films. The typical load–displacement curves of the thin films deposited at various Ar gas flow rates are shown in Figure 7, and the detailed mechanical properties are listed in Table 4. The maximum depth of the films is 1/10 of the thickness of each film. At the same maximum depth, the maximum load would be the highest for the specimen with an Ar gas flow rate of 5 sccm and the lowest for the specimen with an Ar gas flow rate of 8 sccm. Similarly, as presented in Table 4, the specimen with the Ar gas flow rate of 5 sccm had the highest Vickers hardness, with a value of about 1137 HV.

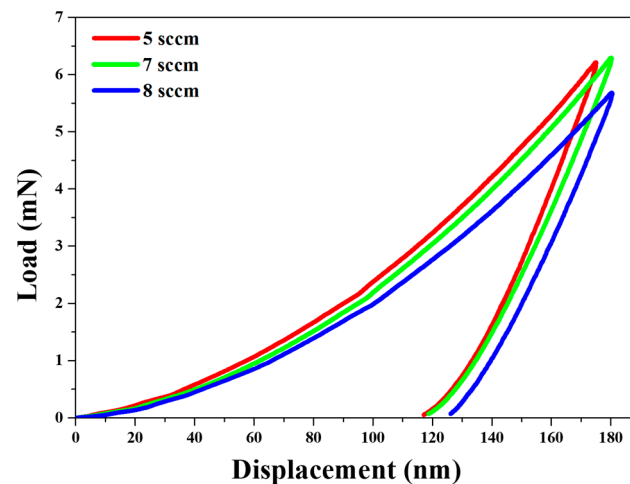


Figure 7. The typical nanoindentation load–displacement curves of AlCoCrNi HEA metallic films deposited at various Ar flow rates.

Table 4. The hardness, elastic modulus, Vickers hardness, and H/E of the AlCoCrNi HEA metallic films deposited at various Ar gas flow rates.

Ar Flow Rate (sccm)	Mechanical Properties			
	H _{IT} (GPa)	E _{IT} (GPa)	HV _{IT} (HV)	H/E
5	12.21 ± 1.05	188.1 ± 11	1137.1 ± 9.2	0.0648 ± 0.0018
7	11.40 ± 1.75	165.2 ± 19	1101.4 ± 15.4	0.0687 ± 0.0027
8	9.05 ± 3.19	141.1 ± 39	943.7 ± 32.5	0.0619 ± 0.0076

As shown in Figures 2 and 4, this difference in mechanical properties is neither caused by a phase transformation nor a difference in chemical composition. Herein, it is the densification of the film by ion bombardment that predominantly affects the mechanical properties. The increase in the mean free path that occurs when the gas flow rate is low during sputtering can improve the force of the collision toward the substrate. The improved collision force can lead to enhanced hardness under the action of high compressive stress [43,45,46]. Also, recent research has used the H/E ratio value to estimate the plastic deformation and wear resistance of coatings [34,47–49]. The high H/E values indicate increased resistance to cracking and plastic deformation by dispersing the applied load across a broader area of the coating [34]. In the case of the AlCoCrNi HEA metallic film deposited with an Ar flow rate of 8 sccm, which is one that where cracking occurred, the H/E ratio showed the lowest value of about 0.0619, as expected. Similarly, in the previous study, among the results of depositing the AlCoCrNi nitride films under various process parameters, nano-scale voids and density deficient boundaries were observed in the nitride film with the lowest H/E value [22]. In addition, the H/E ratio of the nitride thin film with better mechanical properties was about 0.0692 [22], and by comparison the overall H/E value of this study was relatively high.

In this study, all the AlCoCrNi HEA metallic films formed a BCC phase regardless of Ar gas flow rate conditions, but their mechanical properties tended to depend on Ar flow rate conditions. As a result, the AlCoCrNi HEA metallic film with an Ar gas flow rate of 8 sccm exhibited cracks as well as decreased mechanical properties, whereas the other films showed improved mechanical properties and no cracks. In other words, it is possible to remove cracks and improve mechanical properties simultaneously by controlling the gas flow rate. Based on these results, it is believed that the gas flow rate contributes substantially to controlling the surface morphology, microstructures, and mechanical properties of AlCoCrNi HEA metallic films.

4. Conclusions

AlCoCrNi HEA metallic films were deposited using a magnetron sputtering system at room temperature with an Ar gas flow rate adjusted to 5, 7, and 8 sccm. All AlCoCrNi HEA metallic films were identified as being in the BCC phase, with an almost equiatomic percentage chemical composition regardless of the Ar gas flow rate. However, cracks occurred on the surface of the specimen deposited with an Ar gas flow rate of 8 sccm. From the TEM analysis of the specimen deposited with an Ar gas flow rate of 8 sccm, void boundaries were found; it was confirmed that these void boundaries contributed to the cracks and that this was due to the shadowing effect. Conversely, as the Ar gas flow rate decreased, the void boundaries and the cracks on the surface were removed. The Vickers hardness was highest in the specimen with an Ar gas flow rate of 5 sccm at 1147 HV, which was attributed to the fact that the densification via ion bombardment affected the mechanical properties. These results were caused by the increase in the diffusion energy as the mean free path lengthened and the mobility of the particles increased. Consequently, we conclude that cracks were removed from the specimen with poor surface quality by controlling the gas flow rate, and at the same time the mechanical properties were improved.

Author Contributions: Writing—original draft, Y.-S.K. (Young-Soon Kim); Writing—review & editing, H.-J.P.; Methodology, Y.-S.K. (Young-Seok Kim) and H.-J.P.; Investigation, Y.-S.K. (Young-Soon Kim); Data curation, H.-J.P., S.-H.H. and Y.-S.K. (Young-Soon Kim); Formal analysis, Y.-S.K. (Young-Seok Kim) and H.-J.P.; Visualization, H.-J.P.; Conceptualization, K.-B.K.; Supervision, K.-B.K.; Project administration, K.-B.K. and H.-J.P. All authors have read and agreed to the published version of the manuscript.

Funding: This work was supported by the Technology Innovation Program (or Industrial Strategic Technology Development Program-Material Parts Technology Development Project) (20017502, Development of the Carbide/PCBN Cutting tool and the Customized Cutting Solution for High Hardened Steel, by Machine Learning) funded By the Ministry of Trade, Industry & Energy (MOTIE, Korea) and the Basic Science Research Program through the National Research Foundation of Korea (NRF) funded by the Ministry of Education (RS-2023-00250752).

Institutional Review Board Statement: Not applicable.

Informed Consent Statement: Not applicable.

Data Availability Statement: Data are contained within the article.

Conflicts of Interest: Author Young-Seok Kim was employed by the company APIs Co. The remaining authors declare that the research was conducted in the absence of any commercial or financial relationships that could be construed as a potential conflict of interest.

References

1. Cantor, B.; Chang, I.T.H.; Knight, P.; Vincent, A.J.B. Microstructural Development in Equiatomic Multicomponent Alloys. *Mater. Sci. Eng. A* **2004**, *375*, 213–218. [[CrossRef](#)]
2. Yeh, J.-W. Recent Progress in High Entropy Alloys. *Ann. Chim. Sci. Mater.* **2006**, *31*, 633–648.
3. Yan, X.H.; Li, J.S.; Zhang, W.R.; Zhang, Y. A Brief Review of High-Entropy Films. *Mater. Chem. Phys.* **2018**, *210*, 12–19. [[CrossRef](#)]
4. Zhang, Y.; Zhou, Y.J.; Lin, J.P.; Chen, G.L.; Liaw, P.K. Solid-solution Phase Formation Rules for Multi-component Alloys. *Adv. Eng. Mater.* **2008**, *10*, 534–538. [[CrossRef](#)]
5. George, E.P.; Raabe, D.; Ritchie, R.O. High-Entropy Alloys. *Nat. Rev. Mater.* **2019**, *4*, 515–534. [[CrossRef](#)]
6. Park, H.J.; Na, Y.S.; Hong, S.H.; Kim, J.T.; Kim, Y.S.; Lim, K.R.; Park, J.M.; Kim, K.B. Phase Evolution, Microstructure and Mechanical Properties of Equi-Atomic Substituted TiZrHfNiCu and TiZrHfNiCuM (M = Co, Nb) High-Entropy Alloys. *Met. Mater. Int.* **2016**, *22*, 551–556. [[CrossRef](#)]
7. Jumaev, E.; Hong, S.H.; Kim, J.T.; Park, H.J.; Kim, Y.S.; Mun, S.C.; Park, J.-Y.; Song, G.; Lee, J.K.; Min, B.H.; et al. Chemical Evolution-Induced Strengthening on AlCoCrNi Dual-Phase High-Entropy Alloy with High Specific Strength. *J. Alloys Compd.* **2019**, *777*, 828–834. [[CrossRef](#)]
8. Park, H.J.; Kim, Y.S.; Mun, S.C.; Hong, S.H.; Wang, W.-M.; Kim, K.B. Designing of Fe-Containing (Ti₃₃Zr₃₃Hf₃₃)-(Ni₅₀Cu₅₀) High Entropy Alloys Developed by Equiatomic Substitution: Phase Evolution and Mechanical Properties. *J. Mater. Res. Technol.* **2020**, *9*, 7732–7739. [[CrossRef](#)]

9. Pogrebnjak, A.D.; Bagdasaryan, A.A.; Yakushchenko, I.V.; Beresnev, V.M. The Structure and Properties of High-Entropy Alloys and Nitride Coatings Based on Them The Structure and Properties of High-Entropy Alloys and Nitride Coatings Based on Them. *Russ. Chem. Rev.* **2014**, *83*, 1027. [[CrossRef](#)]
10. Kim, H.; Nam, S.; Roh, A.; Son, M.; Ham, M.-H.; Kim, J.-H.; Choi, H. Mechanical and Electrical Properties of NbMoTaW Refractory High-Entropy Alloy Thin Films. *Int. J. Refract. Met. Hard Mater.* **2019**, *80*, 286–291. [[CrossRef](#)]
11. Gorr, B.; Müller, F.; Azim, M.; Christ, H.-J.; Müller, T.; Chen, H.; Kauffmann, A.; Heilmaier, M. High-Temperature Oxidation Behavior of Refractory High-Entropy Alloys: Effect of Alloy Composition. *Oxid. Met.* **2017**, *88*, 339–349. [[CrossRef](#)]
12. Zhou, Y.J.; Zhang, Y.; Wang, Y.L.; Chen, G.L. Solid Solution Alloys of AlCoCrFeNiTi_x with Excellent Room-Temperature Mechanical Properties. *Appl. Phys. Lett.* **2007**, *90*, 181904. [[CrossRef](#)]
13. Huang, Y.-S.; Chen, L.; Lui, H.-W.; Cai, M.-H.; Yeh, J.-W. Microstructure, Hardness, Resistivity and Thermal Stability of Sputtered Oxide Films of AlCoCrCu_{0.5}NiFe High-Entropy Alloy. *Mater. Sci. Eng. A* **2007**, *457*, 77–83. [[CrossRef](#)]
14. Wu, J.-M.; Lin, S.-J.; Yeh, J.-W.; Chen, S.-K.; Huang, Y.-S.; Chen, H.-C. Adhesive Wear Behavior of Al_xCoCrCuFeNi High-Entropy Alloys as a Function of Aluminum Content. *Wear* **2006**, *261*, 513–519. [[CrossRef](#)]
15. Tsai, D.-C.; Chang, Z.-C.; Kuo, B.-H.; Tsao, C.-T.; Chen, E.-C.; Shieu, F.-S. Influence of Discharge Power on the Structural, Electro-Optical, and Mechanical Properties of (TiZrHf)N Coatings. *J. Alloys Compd.* **2015**, *622*, 446–457. [[CrossRef](#)]
16. Jin, H.; Seok, Y.; Hoon, Y.; Hwan, S.; Sik, K.; Koon, Y.; Buem, K. Design of Nano-Scale Multilayered Nitride Hard Coatings Deposited by Arc Ion Plating Process: Microstructural and Mechanical Characterization. *J. Mater. Res. Technol.* **2021**, *15*, 572–581. [[CrossRef](#)]
17. Pierson, H.O. *Handbook of Refractory Carbides & Nitrides: Properties, Characteristics, Processing and Applications*; William Andrew: Norwich, NY, USA, 1996; ISBN 081551770X.
18. Cheng, J.B.; Liang, X.B.; Wang, Z.H.; Xu, B.S. Formation and Mechanical Properties of CoNiCuFeCr High-Entropy Alloys Coatings Prepared by Plasma Transferred Arc Cladding Process. *Plasma Chem. Plasma Process.* **2013**, *33*, 979–992. [[CrossRef](#)]
19. Zhang, C.; Chen, G.J.; Dai, P.Q. Evolution of the Microstructure and Properties of Laser-Clad FeCrNiCoB_x High-Entropy Alloy Coatings. *Mater. Sci. Technol.* **2016**, *32*, 1666–1672. [[CrossRef](#)]
20. Hsieh, M.-H.; Tsai, M.-H.; Shen, W.-J.; Yeh, J.-W. Structure and Properties of Two Al–Cr–Nb–Si–Ti High-Entropy Nitride Coatings. *Surf. Coat. Technol.* **2013**, *221*, 118–123. [[CrossRef](#)]
21. Kim, Y.S.; Park, H.J.; Mun, S.C.; Jumaev, E.; Hong, S.H.; Song, G.; Kim, J.T.; Park, Y.K.; Kim, K.S.; Jeong, S.I.; et al. Investigation of Structure and Mechanical Properties of TiZrHfNiCuCo High Entropy Alloy Thin Films Synthesized by Magnetron Sputtering. *J. Alloys Compd.* **2019**, *797*, 834–841. [[CrossRef](#)]
22. Kim, Y.S.; Park, H.J.; Lim, K.S.; Hong, S.H.; Kim, K.B. Structural and Mechanical Properties of AlCoCrNi High Entropy Nitride Films: Influence of Process Pressure. *Coatings* **2019**, *10*, 10. [[CrossRef](#)]
23. Khan, N.A.; Akhavan, B.; Zhou, C.; Zhou, H.; Chang, L.; Wang, Y.; Liu, Y.; Bilek, M.M.; Liu, Z. High Entropy Nitride (HEN) Thin Films of AlCoCrCu_{0.5}FeNi Deposited by Reactive Magnetron Sputtering. *Surf. Coat. Technol.* **2020**, *402*, 126327. [[CrossRef](#)]
24. Khan, N.A.; Akhavan, B.; Zhou, C.; Zhou, H.; Chang, L.; Wang, Y.; Liu, Y.; Fu, L.; Bilek, M.M.; Liu, Z. RF Magnetron Sputtered AlCoCrCu_{0.5}FeNi High Entropy Alloy (HEA) Thin Films with Tuned Microstructure and Chemical Composition. *J. Alloys Compd.* **2020**, *836*, 155348. [[CrossRef](#)]
25. Khan, N.A.; Akhavan, B.; Zhou, H.; Chang, L.; Wang, Y.; Sun, L.; Bilek, M.M.; Liu, Z. High Entropy Alloy Thin Films of AlCoCrCu_{0.5}FeNi with Controlled Microstructure. *Appl. Surf. Sci.* **2019**, *495*, 143560. [[CrossRef](#)]
26. Liao, W.; Lan, S.; Gao, L.; Zhang, H.; Xu, S.; Song, J.; Wang, X.; Lu, Y. Nanocrystalline High-Entropy Alloy (CoCrFeNiAl_{0.3}) Thin-Film Coating by Magnetron Sputtering. *Thin Solid Film.* **2017**, *638*, 383–388. [[CrossRef](#)]
27. Karunasiri, R.P.U.; Bruinsma, R.; Rudnick, J. Thin-Film Growth and the Shadow Instability. *Phys. Rev. Lett.* **1989**, *62*, 788–791. [[CrossRef](#)] [[PubMed](#)]
28. Salvalaglio, M.; Backofen, R.; Voigt, A. Thin-Film Growth Dynamics with Shadowing Effects by a Phase-Field Approach. *Phys. Rev. B* **2016**, *94*, 235432. [[CrossRef](#)]
29. Hu, M.; Cao, Q.P.; Wang, X.D.; Zhang, D.X.; Jiang, J.-Z. Tuning Nanostructure and Mechanical Property of Fe–Co–Ni–Cr–Mn High-Entropy Alloy Thin Films by Substrate Temperature. *Mater. Today Nano* **2021**, *15*, 100130. [[CrossRef](#)]
30. Yao, W.; Cao, Q.P.; Liu, S.Y.; Wang, X.D.; Fecht, H.-J.; Caron, A.; Zhang, D.X.; Jiang, J.Z. Tailoring Nanostructured Ni–Nb Metallic Glassy Thin Films by Substrate Temperature. *Acta Mater.* **2020**, *194*, 13–26. [[CrossRef](#)]
31. Cemin, F.; de Mello, S.R.S.; Figueroa, C.A.; Alvarez, F. Influence of Substrate Bias and Temperature on the Crystallization of Metallic NbTaTiVZr High-Entropy Alloy Thin Films. *Surf. Coat. Technol.* **2021**, *421*, 127357. [[CrossRef](#)]
32. Ali, A.M.; Egiza, M.; Murasawa, K.; Sugita, H.; Deckert-Gaudig, T.; Deckert, V.; Yoshitake, T. Effects of Substrate Temperature and Intermediate Layer on Adhesion, Structural and Mechanical Properties of Coaxial Arc Plasma Deposition Grown Nanodiamond Composite Films on Si Substrates. *Surf. Coat. Technol.* **2021**, *417*, 127185. [[CrossRef](#)]
33. Rajalekshmi, E.S.; Raj, A.M.E. Effect of Substrate Temperature on Structural and Morphological Studies by Spray Pyrolysed ZnO Thin Films. *Solid State Commun.* **2021**, *338*, 114479. [[CrossRef](#)]
34. Lim, K.S.; Kim, Y.S.; Hong, S.H.; Song, G.; Kim, K.B. Influence of N₂ Gas Flow Ratio and Working Pressure on Amorphous Mo–Si–N Coating during Magnetron Sputtering. *Coatings* **2020**, *10*, 34. [[CrossRef](#)]
35. Clemens, B.M. Effect of Sputtering Pressure on the Structure and Solid-state Reaction of Titanium-nickel Compositionally Modulated Film. *J. Appl. Phys.* **1987**, *61*, 4525–4529. [[CrossRef](#)]

36. Bundesmann, C.; Feder, R.; Gerlach, J.W.; Neumann, H. Ion Beam Sputter Deposition of Ag Films: Influence of Process Parameters on Electrical and Optical Properties, and Average Grain Sizes. *Thin Solid Film.* **2014**, *551*, 46–52. [[CrossRef](#)]
37. Oliver, W.C.; Pharr, G.M. An Improved Technique for Determining Hardness and Elastic Modulus Using Load and Displacement Sensing Indentation Experiments. *J. Mater. Res.* **1992**, *7*, 1564–1583. [[CrossRef](#)]
38. Tsai, D.-C.; Chang, Z.-C.; Kuo, B.-H.; Chen, B.-C.; Chen, E.-C.; Shieu, F.-S. Wide Variation in the Structure and Physical Properties of Reactively Sputtered (TiZrHf)N Coatings under Different Working Pressures. *J. Alloys Compd.* **2018**, *750*, 350–359. [[CrossRef](#)]
39. Moon, Y.-K.; Bang, B.; Kim, S.-H.; Jeong, C.-O.; Park, J.-W. Effects of Working Pressure on the Electrical and Optical Properties of Aluminum-Doped Zinc Oxide Thin Films. *J. Mater. Sci. Mater. Electron.* **2008**, *19*, 528–532. [[CrossRef](#)]
40. Li, W.; Liu, P.; Liaw, P.K. Microstructures and Properties of High-Entropy Alloy Films and Coatings: A Review. *Mater. Res. Lett.* **2018**, *6*, 199–229. [[CrossRef](#)]
41. Cheng, K.-H.; Lai, C.-H.; Lin, S.-J.; Yeh, J.-W. Structural and Mechanical Properties of Multi-Element (AlCrMoTaTiZr) N_x Coatings by Reactive Magnetron Sputtering. *Thin Solid Film.* **2011**, *519*, 3185–3190. [[CrossRef](#)]
42. Yamamura, Y.; Tawara, H. Energy Dependence of Ion-Induced Sputtering Yields from Monatomic Solids at Normal Incidence. *At. Data Nucl. Data Tables* **1996**, *62*, 149–253. [[CrossRef](#)]
43. Cullity, B.D. *Elements of X-ray Diffraction*; Addison-Wesley Publishing: Boston, MA, USA, 1956.
44. Tsai, D.-C.; Huang, Y.-L.; Lin, S.-R.; Liang, S.-C.; Shieu, F.-S. Effect of Nitrogen Flow Ratios on the Structure and Mechanical Properties of (TiVCrZrY)N Coatings Prepared by Reactive Magnetron Sputtering. *Appl. Surf. Sci.* **2010**, *257*, 1361–1367. [[CrossRef](#)]
45. Su, Y.D.; Hu, C.Q.; Wen, M.; Wang, C.; Liu, D.S.; Zheng, W.T. Effects of Bias Voltage and Annealing on the Structure and Mechanical Properties of WC_{0.75}N_{0.25} Thin Films. *J. Alloys Compd.* **2009**, *486*, 357–364. [[CrossRef](#)]
46. Rickerby, D.S.; Burnett, P.J. Correlation of Process and System Parameters with Structure and Properties of Physically Vapour-Deposited Hard Coatings. *Thin Solid Film.* **1988**, *157*, 195–222. [[CrossRef](#)]
47. Musil, J.; Kunc, F.; Zeman, H.; Polakova, H. Relationships between Hardness, Young's Modulus and Elastic Recovery in Hard Nanocomposite Coatings. *Surf. Coat. Technol.* **2002**, *154*, 304–313. [[CrossRef](#)]
48. Leyland, A.; Matthews, A. On the Significance of the H/E Ratio in Wear Control: A Nanocomposite Coating Approach to Optimised Tribological Behaviour. *Wear* **2000**, *246*, 1–11. [[CrossRef](#)]
49. Musil, J. Hard Nanocomposite Coatings: Thermal Stability, Oxidation Resistance and Toughness. *Surf. Coat. Technol.* **2012**, *207*, 50–65. [[CrossRef](#)]

Disclaimer/Publisher's Note: The statements, opinions and data contained in all publications are solely those of the individual author(s) and contributor(s) and not of MDPI and/or the editor(s). MDPI and/or the editor(s) disclaim responsibility for any injury to people or property resulting from any ideas, methods, instructions or products referred to in the content.